# A neural network reconstruction approach for obtaining parallax-free X-ray powder diffraction computed tomography data from large samples

Dong H.[a,b], Jacques S.D.M.[b], Butler K.T.[c, a], Gutowski O.[d], Dippel A.C.[d], von Zimmerman M.[d], Beale A.M.[a,b,e], Vamvakeros A.[b,f]*

a) Department of Chemistry, University College London, 20 Gordon Street, London WC1H 0AJ, United Kingdom

b) Finden Limited, Merchant House, 5 East St Helens Street, Abingdon, OX14 5EG, United Kingdom

c) SciML, Scientific Computer Division, Rutherford Appleton Laboratory, Harwell OX11 0QX, United Kingdom

d) Deutsches Elektronen-Synchrotron DESY, Notkestraße 85, 22607 Hamburg, Germany

e) Research Complex at Harwell, Rutherford Appleton Laboratory, Harwell Science and Innovation Campus, Didcot, Oxon OX11 0FA, United Kingdom

f) Dyson School of Design Engineering, Imperial College London, London SW7 2DB, United Kingdom

*correspondence email: antony@finden.co.uk

## Abstract

In this study, we introduce an innovative method designed to eliminate parallax artefacts present in X-ray powder diffraction computed tomography data acquired from large samples. Our approach integrates a unique 3D neural network architecture with a forward projector that accounts for the experimental geometry. This self-supervised technique for tomographic volume reconstruction is designed to be chemistry-agnostic, eliminating the need for prior knowledge of the sample's chemical composition. We showcase the efficacy of this method through its application on both simulated and experimental X-ray diffraction tomography data, acquired from a phantom sample and a commercially available and industrially relevant NMC532 cylindrical Lithium-ion battery.

## Introduction

Deep learning, an advanced subset of machine learning, has been a game-changer across a diverse array of fields, including image recognition and text translation [1–6]. Unlike traditional 'hand-crafted' algorithms that operate on fixed principles, deep learning harnesses flexible neural networks that evolve based on exposure to existing examples. This dynamic, data-driven, learning process allows deep learning models to continually refine their performance, driving significant advancements in complex tasks where flexibility and adaptability are key.

One of the key areas that deep learning has made a significant impact is in the field of tomographic image reconstruction [7–9]. Traditionally, tomographic image reconstruction has relied on either direct methods, like the filtered back projection (FBP) algorithm [10], or iterative methods that depend on prior knowledge and fine-tuning. However, these methods face their own limitations, especially when it comes to scalability, handling noise and angular undersampling data, computational demand, and the necessity for absolute values in certain applications [11–13]. Deep neural networks (DNNs) have emerged as a compelling solution, offering the potential to surpass the performance of these traditional physics-based approaches [14–16].

In recent years, there has been a burgeoning interest in the application of DNNs in tomography, notably in enhancing the quality of real-space reconstructed images generated from sinograms. Besides, some innovative applications even leverage supervised learning and generative models to automatically map from sinogram to real space [17–24]. Despite certain bottlenecks such as handling large images and the computational cost of large networks, the promise of deep learning in this sphere is quite palpable.

The advent of X-ray (powder) diffraction computed tomography (XRD-CT), a specialized form of tomography, has added a new dimension to the mix. This technique uses a pencil beam scanning method to yield reconstructed images corresponding to a sample's cross-section [25–27]. What sets XRD-CT apart is its ability to resolve chemical species of similar density, a task that conventional X-ray CT often struggles with. As such, XRD-CT has found applications in a wide array of fields ranging from material science to cultural heritage conservation, as well as biological samples [28,29]. More importantly, XRD-CT has become an invaluable tool to investigate, non-destructively, functional materials and devices, such catalytic reactors [30–36], fuel cells [37,38] and secondary/rechargeable batteries in custom made laboratory cells [38–43] as well as in commercially available and industrially relevant cylindrical form [44–46], under static or operating conditions (*in situ/ operando* studies). These studies have shown that the spatially-resolved diffraction patterns in the XRD-CT data can yield unique physicochemical information regarding these complex materials systems and their evolving solid-state chemistry. Recently, the method has also been demonstrated for five dimensional (5D) experiments, where the dimensions correspond to three spatial, one chemical (diffraction) and one temporal or imposed operating condition *(e.g.* temperature, pressure, potential) [47–49].

Given the prowess of deep learning and the unique capabilities of XRD-CT, the combination of these two could potentially revolutionize tomographic image reconstruction. Deep learning methods could not only accelerate the XRD-CT on both data acquisition and analysis but also enhance it by addressing challenges like image super-resolution using high resolution region-of-interest CT scans, data denoising, as well as single-crystal diffraction, self-absorption and parallax artefacts. This combination, if realized, could unlock new possibilities, including

higher spatial and temporal resolution in chemical imaging and better handling of complex data sets, paving the way for breakthroughs in various fields.

One major obstacle that prohibits the scale up of the XRD-CT technique and its widespread adoption to study large samples is the parallax artefact. In wide angle scattering-based CT experiments, it is generally assumed that the X-rays, whether scattered or diffracted, arrive at the same detector element when measured at any given scattering angle 2θ across the sample's thickness, as depicted in Figure 1a. This assumption holds when the sample thickness is relatively small, typically on the order of a few millimeters. However, for thicker samples, this assumption becomes invalid. In these cases, diffracted X-rays measured at a specific 2θ angle are detected by multiple detector elements due to the significantly varying distances between elements within the sample and the detector. This phenomenon, known as the parallax effect, exhibits a tan(2θ) dependency [25,27]. The parallax effect is further illustrated in Figure 1b. As a result of this effect, artefacts may manifest as shifts in peak position, peak broadening, or even peak splitting [50].
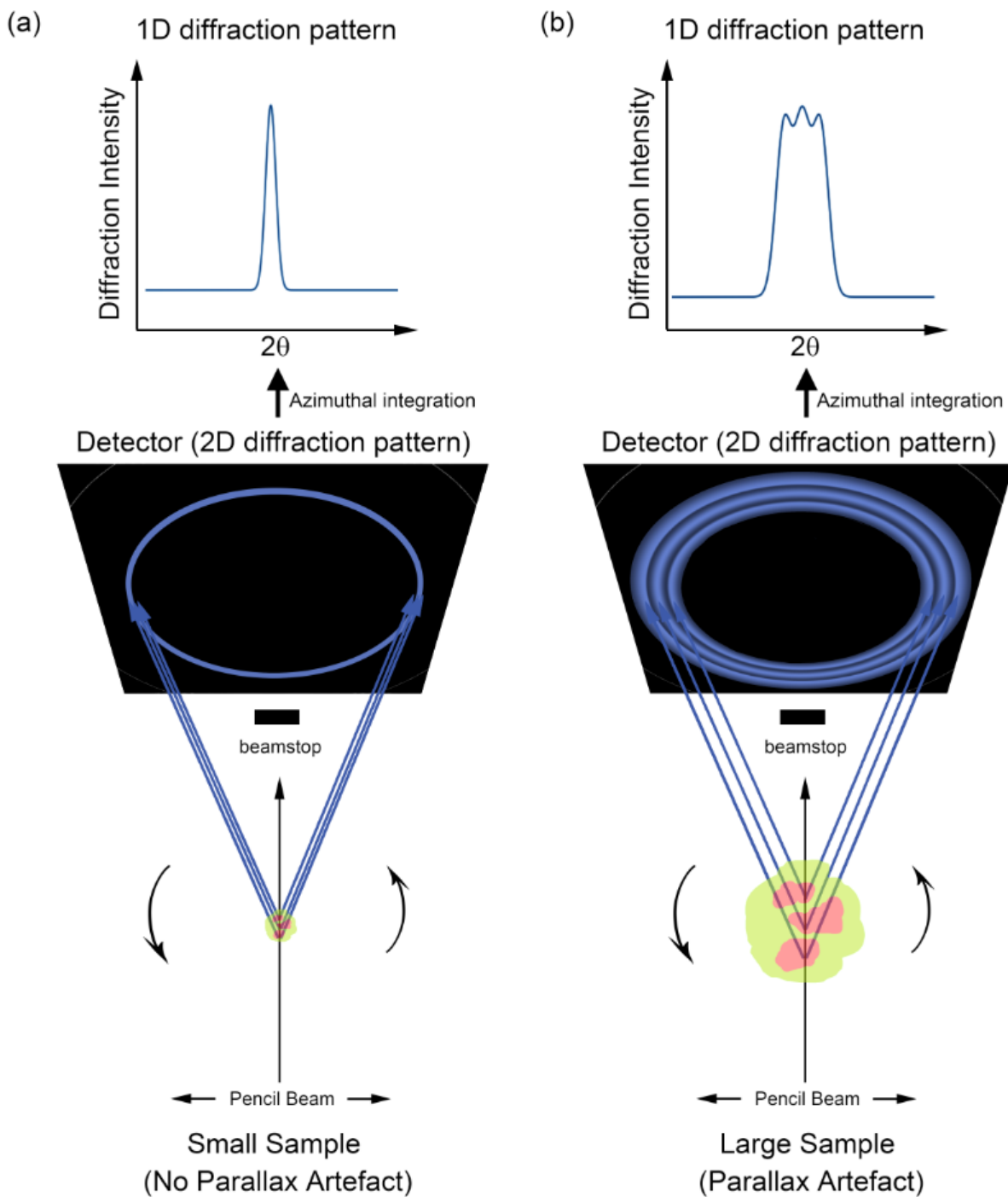
Figure 1. (a) Schematic representation of a 2D XRD pattern collected during the XRD-CT scanning of a small sample when there is no parallax artefact. (b) 2D XRD pattern collected during the XRD-CT scanning of a large sample with parallax artefacts present; the X-rays scattered/diffracted along the sample at certain 2θ angles arrive at different detector elements, leading to peak broadening and peak splitting.

In our previous work, we developed a new reconstruction approach, termed "direct least-squares reconstruction" (DLSR) algorithm, which overcomes the parallax artefact in XRD-CT data [51]. Conventionally, the XRD-CT sinogram data are reconstructed one-by-one, typically using the filtered back projection algorithm, yielding an XRD-CT reconstructed volume. The next step involves the analysis of all the local diffraction patterns in this reconstructed XRD-CT volume which can be single, multi-peak fitting or full profile analysis using methods such as LeBail or Rietveld. The DLSR was implemented using the TOPAS software [52] version 7 and combines the reconstruction and full profile analysis steps into a single step. To clarify, the sinogram XRD-CT (projection) data are fitted and the results are real-space maps corresponding to the various properties of the model that is being refined (*e.g.* scale factor, lattice parameter and crystallite size maps for each phase). This approach yields parallax artefact-free images but has severe limitations:

- It requires *a priori* knowledge about the chemistry of the sample before reconstruction
- It requires the construction of a robust physical model that models all chemistry accurately in the sinogram data; minor components being overlooked during the inspection of diffraction patterns when preparing the physical model will not be part of the final results
- DLSR in its TOPAS version 7 implementation suffers from scalability; even XRD-CT images that are nowadays considered standard (*e.g.* 256 x 256) cannot be handled due to RAM requirements and the data have to be rebinned losing spatial resolution.
- It typically requires laborious data pre-processing to decrease memory requirements (to that realistically available) and yield stable reconstructions. For example, one needs to create a separate binary mask for each crystalline phase present by analysing the FBP reconstructed XRD-CT volume (which contains parallax artefacts) and/or subtract the background from the sinogram data (in order to make it linear/ use a simple background model)

Therefore, our motivation was to develop a new method that overcomes all these limitations of the DLSR approach and yield parallax artefact-free XRD-CT images.


## Self-supervised parallax artefact removal

We developed a self-supervised parallax XRD-CT data reconstruction architecture by integrating a forward operator that can transfer an XRD-CT volume without parallax artefacts to the sinograms with parallax artefacts. A schematic representation of the method is shown in Figure 2. We use an artificial neural network which acts as an XRD-CT volume generator i.e. it creates a stack of real-space XRD-CT images. The input to the generator is a random non-zero constant. Next, the generated images are converted into sinograms with the addition of parallax artefacts using a differentiable forward operator. The forward operator contains two parts, the first part

adds artificial parallax artefacts into the images by taking into account the geometry of the experimental setup, and the second part is the Radon transformation that can convert the images to sinograms. This generated XRD-CT sinogram volume is then compared with the experimental sinogram dataset using a designated loss function. Based on this comparison, the weights of the generator network are updated accordingly.
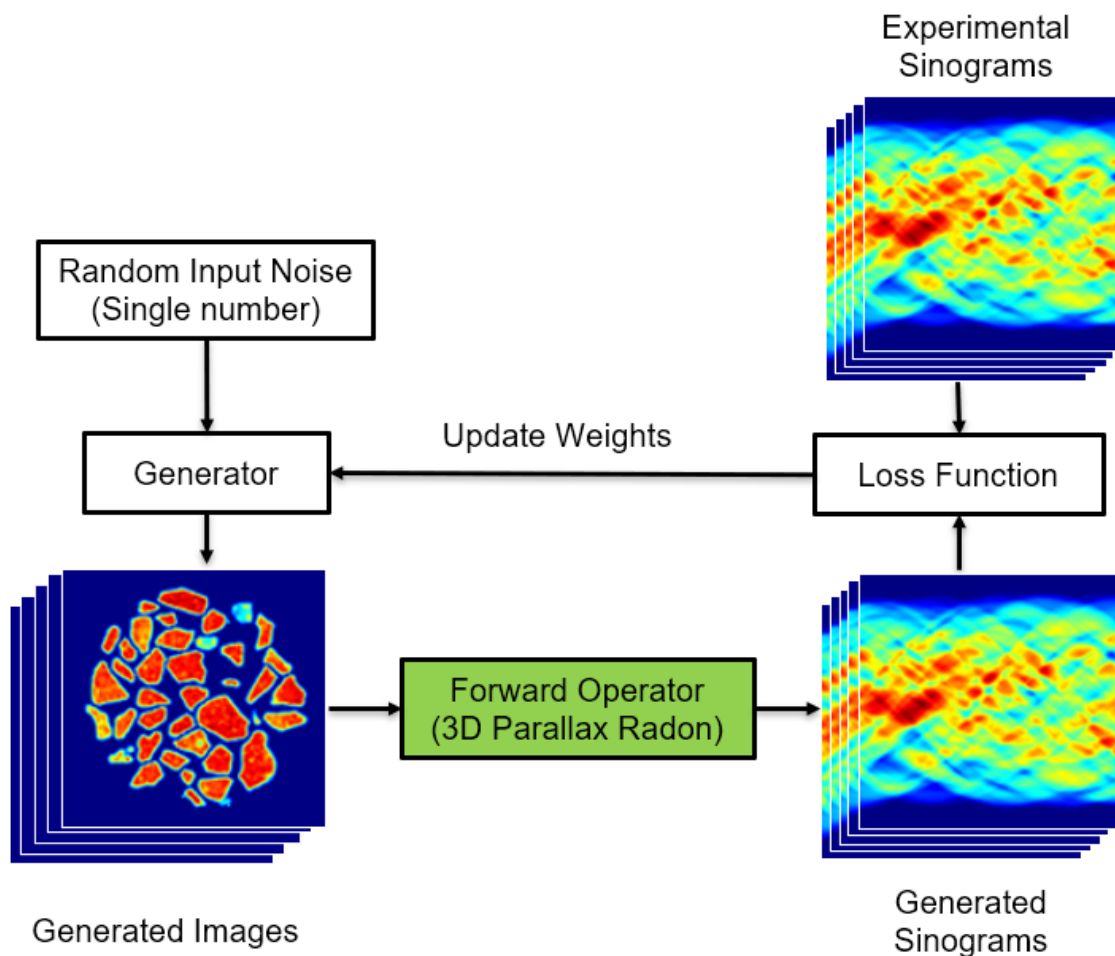


Figure 2. The self-supervised ParallaxNet flow chart. The generator network takes a single-digit number as input and outputs a volume (stack of images), where the third dimension corresponds to the scattering angles (diffraction dimension). A forward operator is applied to convert these XRD-CT images into sinograms containing parallax artefacts. A loss function is then used to compare the differences between the generated sinograms and the experimental sinograms.

Building on the recently developed SD2I architecture[53], which is a lightweight and scalable CNN architecture that utilizes a single number input for CT image reconstruction and addresses angular undersampling artefacts, we introduce the Single Digit to Volume (SD2Vol) network

architecture for enhanced volumetric reconstructions. By transitioning from 2D to 3D convolutional layers and reducing layer parameters, SD2Vol offers both tailored 3D capability and greater efficiency, marking a significant step forward in CT image reconstruction. Figure 3 illustrates the design of the SD2Vol network employed for 3D image reconstruction from a sinogram volume (stack).

The SD2Vol network begins with a single seed input value (specifically, 1 is used in this work), and is followed by a decoder to reconstruct the image based on the single number. After the input layer, three fully connected layers with 32 nodes and another fully connected layer where the number of nodes equal to the total number of voxels in the reconstructed volume are used. Next, the output of the final fully connected layer is reshaped to a 3D volume followed by four 3D convolutional layers. All activation functions are chosen as ReLU, except for the last layer we used the linear activation function. This architecture can be scaled up, as it allows to reconstruct volumes with $n \times n \times m$ sizes reaching 550 x 550 x 51 or 100 x 100 x 4010 (i.e. projection data with parallax artefacts). The maximum size of a volume that ParallaxNet can reconstruct with SD2Vol is presented in Figure S1, and Table S1-S4.
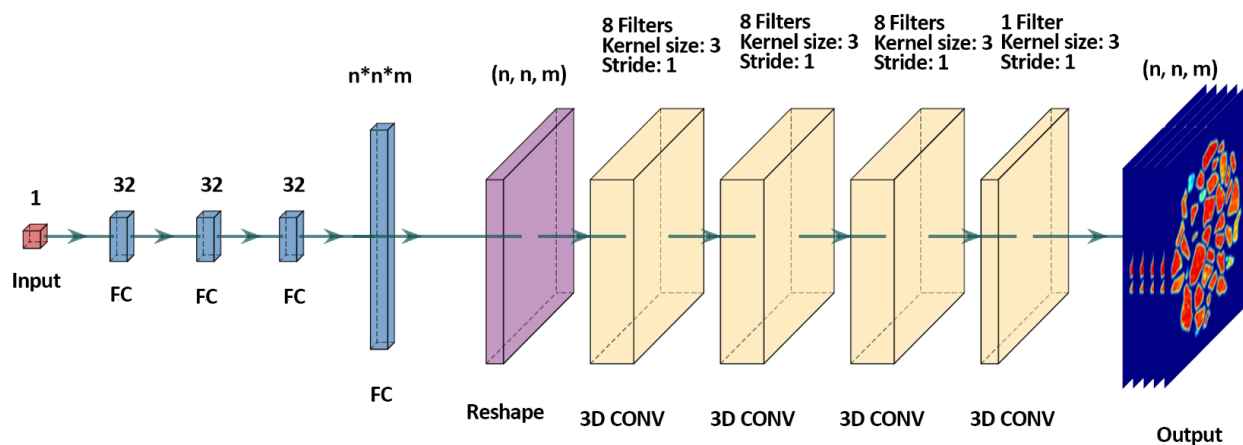


Figure 3. The Single Digit to Volume (SD2Vol) generator architecture with a single constant as input. CONV represents 3-D convolutional layers, and FC represents fully connected layers. The filter numbers and layer sizes are shown above each layer. Here n represents the number of translation steps, and m represents the volume size of the output image. The ReLU function is used to connect the layers, except the Leaky ReLU function is used on the last fully connected layer to adapt possible negative values generated.

We use a joint loss function with the mean squared error (MSE) and the structural similarity index measure (SSIM) in this architecture. The loss function compares the real experimental sinograms with the generated sinograms and updates the weights in the generator to give a

generated sinogram volume that resembles better the experimental sinogram volume on the iteration. Normally, the architecture can yield high quality reconstructions after 1000 iterations. We tested various loss functions, including MSE, mean absolute error (MAE), SSIM, and a joint loss function that combines MSE and SSIM. These tests were conducted with ParallaxNet on the simulated XRD-CT dataset used in this work. The results are presented in Table S5. Based on these findings, we chose the joint loss function that combines MSE and SSIM as the loss function to be used for ParallaxNet. The reconstruction process of this self-supervised method can be expressed as:

$$G(a) = arg\ min\ \ \lambda\ L_{MSE} + (1 - \lambda)L_{SSIM}$$

Here, *G(a)* is the generated reconstruction image by sending a random constant 'a' into the generator. The constant doesn't change while training. The $L_{MSE}$ and $L_{SSIM}$ represent the MSE loss and SSIM loss respectively, and their sum is adjusted by the fraction λ. According to Table S5, we used λ = $10^{-4}$ for all the reconstructions presented in this work.

The MSE loss is defined as [54]:

$$L_{MSE}(\mathbf{x}, \mathbf{y}) = \frac{1}{ntr \times npr \times nim} \sum_{i=0}^{ntr} \sum_{j=0}^{npr} \sum_{k=0}^{nim} \left|\left| \mathbf{x}_{ijk} - \mathbf{y}_{ijk} \right|\right|^2$$

The *ntr, npr* and *nim* represent the number of translation steps, the number of projections, and the volume size (number of channels), respectively. Then, the SSIM loss can be expressed as [55]:

$$L_{SSIM}(\mathbf{x}, \mathbf{y}) = \frac{(2\mu_x\mu_y + C_1)(2\sigma_{xy} + C_2)}{(\mu_x^2 + \mu_y^2 + C_1)(\sigma_x^2 + \sigma_y^2 + C_2)}$$

Here,

$$C_1 = (K_1 L)^2$$
$$C_1 = (K_2 L)^2$$
$$\sigma_{xy} = \frac{1}{N-1} \sum_{i=1}^{N} (x_i - \mu_x)(y_i - \mu_y)$$

The $\mu_x$, $\mu_y$ are the average of all pixels in the input sinograms and the $\sigma_x$, $\sigma_y$ represent their standard deviations. *L* is the dynamic range of the input images. $K_1$ and $K_2$ are two constants that are set as 0.01 and 0.03.

To account for the varying signal strengths across each chemical (diffraction/scattering angle) channel and facilitate easier training of the generator, all sinogram channels along the 2θ axis are normalized based on the maximum value of each channel. Additionally, to ensure the output images from the generator maintain a consistent relative intensity, they are divided by the same normalization factors used for the sinograms before applying the forward operator. Then the forward operator processes images at their actual intensity scale, yielding generated sinograms with accurate intensities. Subsequently, these generated sinograms are multiplied by the normalization factors and the loss is calculated in comparison to the normalized input reference sinograms.

A circular mask is applied to the images during training to filter out signals outside the CT reconstruction area. The 3D grid is calculated considering the experimental setup and specifically the 2θ diffraction angles (1D vector), the sample-to-detector distance, the translation step size and the X-ray wavelength. Starting with a tomographic angle of 0 °, the forward operator accounts for nT voxels across the sample's thickness, and simulates the parallax effect with an nT 2θ axis vector yielding the 3D grid. The modeling of the 3D grid is based on a relationship between the new 2θ axis, its offset from the centre of rotation, and the distance from the sample to the detector, as defined by Scarlett et al. [50] :

$$sin(2\theta_{new}) = -u(y) \times \frac{sin(2\theta_{middle})}{Rs}$$

The sinogram volume with parallax can be created from parallax-free images by rotating the 3D grid, interpolating the XRD-CT data over it, and calculating the 3D Radon transform at each CT angle. The pseudocode for creating the 3D grid based on the experimental setup can be found in Algorithm 1, while the pseudocode for the forward operator is in Algorithm 2.

---

**Algorithm 1: Pseudocode - Creating 3D grid**

1  npix ← number of translation steps
2  npr ← number of projections
3  srange ← npix * translation_step_size
4  Rs ← sample_to_detector_size / cos(two_theta)
5  3D_grid ← Empty List with size (npix, npix, two_theta)
6  **for** *i in range (npr)* **do**
7     xoffs ← (round(npix/2) - (i + 1)) * translation_step_size
8     **for** *j in range (npix)* **do**
9        3D_grid[i,j,:] = two_theta + arcsin(sin(two_theta) * xofs / Rs)
10  **Return** *3D_grid*

---

---

**Algorithm 2: Pseudocode - Parallax forward operating algorithm**

1  Images ← Images * mask
    /* Crop all values outside the circular bound */
2  sinograms ← Empty List
3  grid_3D ← create_grid(twotheta, sample_to_detector_distance, wavelength, translation_step_size)
4  **for** $i$ *in range* ($npr$) **do**
5    | grid_3D_rot ← rotate(grid_3D, theta[i])
6    | Volume ← interpolate(Images, grid_3D_rot)
7    | s ← 3D_Radon_transform(Volume)
8  sinograms ← stack(s)
9  **Return** *sinograms*

---

## Results & Discussion

### Simulated XRD-CT data

To test the performance of ParallaxNet on XRD-CT data with parallax artefacts, we first use a simulated XRD-CT dataset with noiseless and zero-background XRD patterns of a Ni fcc structure (ICSD: 64989) [53]. When testing the performance of algorithms designed to solve inverse problems, it's crucial to ensure the forward projector used to generate simulated data is different from the forward projector the algorithm employs to solve the inverse problem. This differentiation helps maintain the rigor and validity of the evaluation. Being conscious of this, we coded different forward models for testing our approach with the simulated XRD-CT data. Specifically, we used an A matrix (ray tracing) calculated from astra-toolbox [56] as the forward projector to produce the simulated Ni XRD-CT dataset and a custom Radon using image rotation with bilinear interpolation for our ParallaxNet algorithm. This approach ensures a more unbiased assessment of ParallaxNet's capabilities.

We take into account the non-constant sample-to-detector distance for large samples by creating a 3D grid, where each pixel represents a distinct 2θ axis. The XRD-CT data, both the simulated and the experimental presented in the following sections, are interpolated using this 3D grid and subsequently their 3D Radon transform is calculated. The simulated data were created using a sample-to-detector distance of 1000 mm, translation step size of 0.2 mm, and a 100 keV X-ray energy. The simulated XRD-CT data consist of 121 translation steps, 121 projections covering 0-180 ° angular range and 2000 scattering angles, which form a sinogram

volume with the size 121 x 121 x 2000. ParallaxNet was used to reconstruct the whole dataset in ca. 7.4 h and 5000 epochs.

Figure 4 shows the results obtained from the sequential Rietveld analysis of both FBP and ParallaxNet reconstructed volumes using the TOPAS software which is guided by inhouse developed Python scripts. As presented in Figure 4, compared to the Rietveld analysis results of the FBP volume, the maps of Ni scale factor, crystallite size, and lattice parameter *a* from ParallaxNet are almost identical to the ground truth maps while the FBP significantly diverge; this is apparent when one observes the lattice parameter and crystallite size maps. This suggests that the diffraction peak positions and shapes reconstructed by ParallaxNet closely match the ground truth patterns. The differences between the crystallite size and lattice parameter maps and their ground truth values are presented in Figure S2. Their accuracy is also confirmed by the $R_{wp}$ maps from the Rietveld analysis and the distribution of lattice parameters for all pixels, as shown in Figure S3. The mean image and diffraction patterns, along with selected channels of maps, are shown in Figure S4. By visually inspecting the maps reconstructed by FBP and ParallaxNet, we can conclude that ParallaxNet accurately reconstructs the signals in the correct positions and addresses the parallax artefacts present in the simulated data. The distribution of lattice parameters obtained by the three methods are shown in Figure S5.
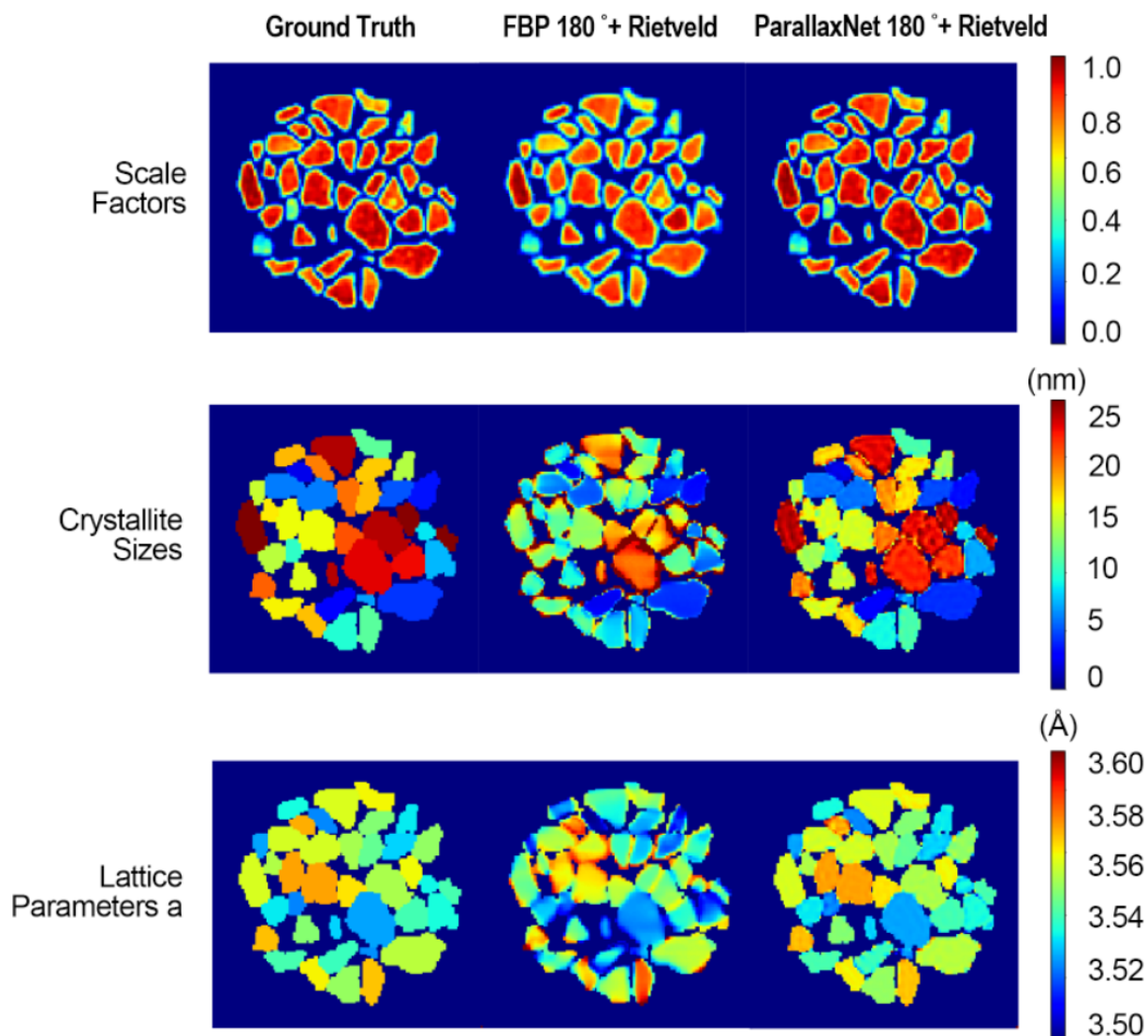
Figure 4. Parallax XRD-CT simulations. This figure shows the results obtained from the sequential Rietveld analysis of the reconstructed XRD-CT data with FBP and ParallaxNet and their ground truth value.

In a pixel-wise analysis, we select three regions of interest as depicted in Figure 5. It can be seen that within each region, the lattice parameter and crystallite size have the same value in the simulated dataset. As illustrated in Figure 5, the parallax artefact causes the FBP reconstructed patterns to exhibit significant shifts in peak positions, broadening, and some instances of splitting when reconstructed using the conventional 0-180 ° CT acquisition. However, the ParallaxNet can accurately reconstruct the volume without these artefacts and the reconstructed diffraction peaks are well aligned with the ground truth.
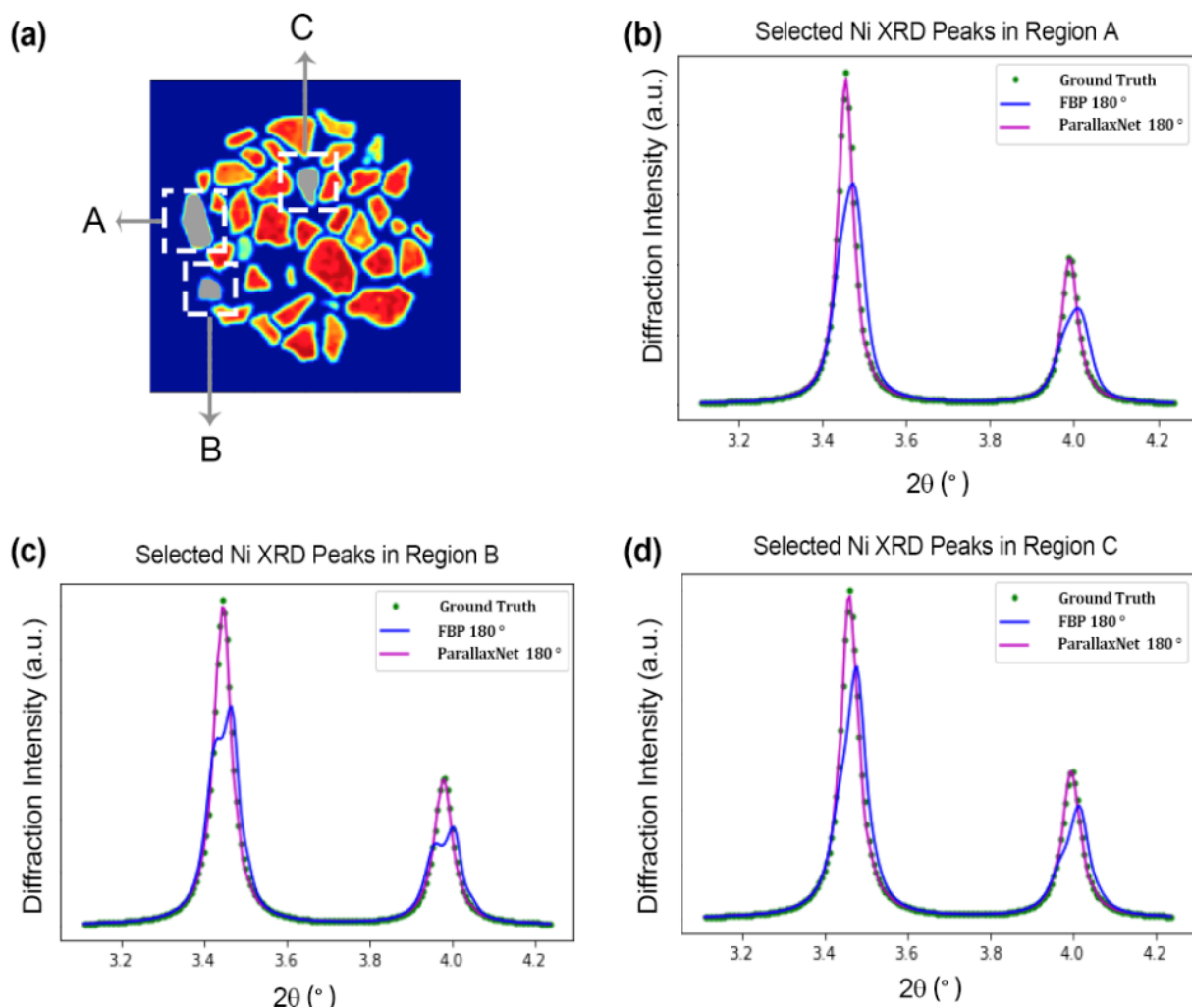
Figure 5. (a) The mean image of the simulated Ni XRD-CT dataset with three marked regions. (b) Selected diffraction peaks of the average diffraction pattern in Region A. (c) Selected peaks of the average diffraction pattern in Region B. (d) Selected peak from average diffraction pattern in Region C. This figure shows the ParallaxNet correctly solving the diffraction peak splitting and shifting caused by parallax artefacts and that the diffraction pattern is aligned with the ground truth one.

## Experimental XRD-CT data

## Phantom

Next, we evaluate the efficacy of the method using experimental XRD-CT data. The first dataset is a custom-made phantom consisting of four pipettes filled with different powder samples [51]. The mean image of the phantom XRD-CT sample can be found in Figure 6a, which provides a

view of the cross-section containing the powder samples within the four glass pipettes. This dataset contains two crystalline MgO (ICSD 9863; Sasaki et al., 1979), one SiC (ICSD 603798; Li & Bradt, 1986) and one $TiO_2$ rutile (ICSD 33837; Sugiyama & Take´uchi, 1991) phases respectively. Figure 6b presents the mean diffraction patterns derived from both FBP and ParallaxNet using 180 ° scans. It can be seen that the diffraction peaks in the FBP pattern are significantly broader compared to the ParallaxNet. Selected channels from the reconstructed XRD-CT dataset are depicted in Figure 6c. It can be clearly seen that the new approach reconstructs artefact-free images while the conventional FBP method displays pronounced parallax artefacts that are readily observable upon visual inspection.

Unlike the dataset presented in our DLSR work, here we utilise the full size of the image dataset with ParallaxNet without any image rebinning/resizing. This is because the new ParallaxNet method boasts better scalability compared to DLSR. The XRD-CT sinogram volume dataset comprises 269 translation steps, 300 projections, and 670 selected diffraction channels. We split the dataset into three batches, and each batch contains 250 channels. To mitigate the edge effect between the batches, we incorporated an overlap of 40 channels for each batch. As a result, the three batches are defined with channel numbers 0-250, 210-460, and 420-670, respectively. The three batches are merged afterwards by taking the average of the overlapped channels.

For each batch, we ran 5,000 epochs, which took ca. 5.28 h excluding the initialization time. To improve image quality and reduce the number of required epochs, we pre-trained the generator using FBP images from 180 ° projections. This preliminary step required only 1,000 iterations and was completed in 4 min for each batch. In total, the image reconstruction with ParallaxNet took ca. 16.43 h. The ParallaxNet training was performed using a workstation equipped with an NVIDIA Quadro RTX8000 GPU, Intel Xeon W-2155 CPU at 3.30GHz and using PyTorch version 1.13.1.
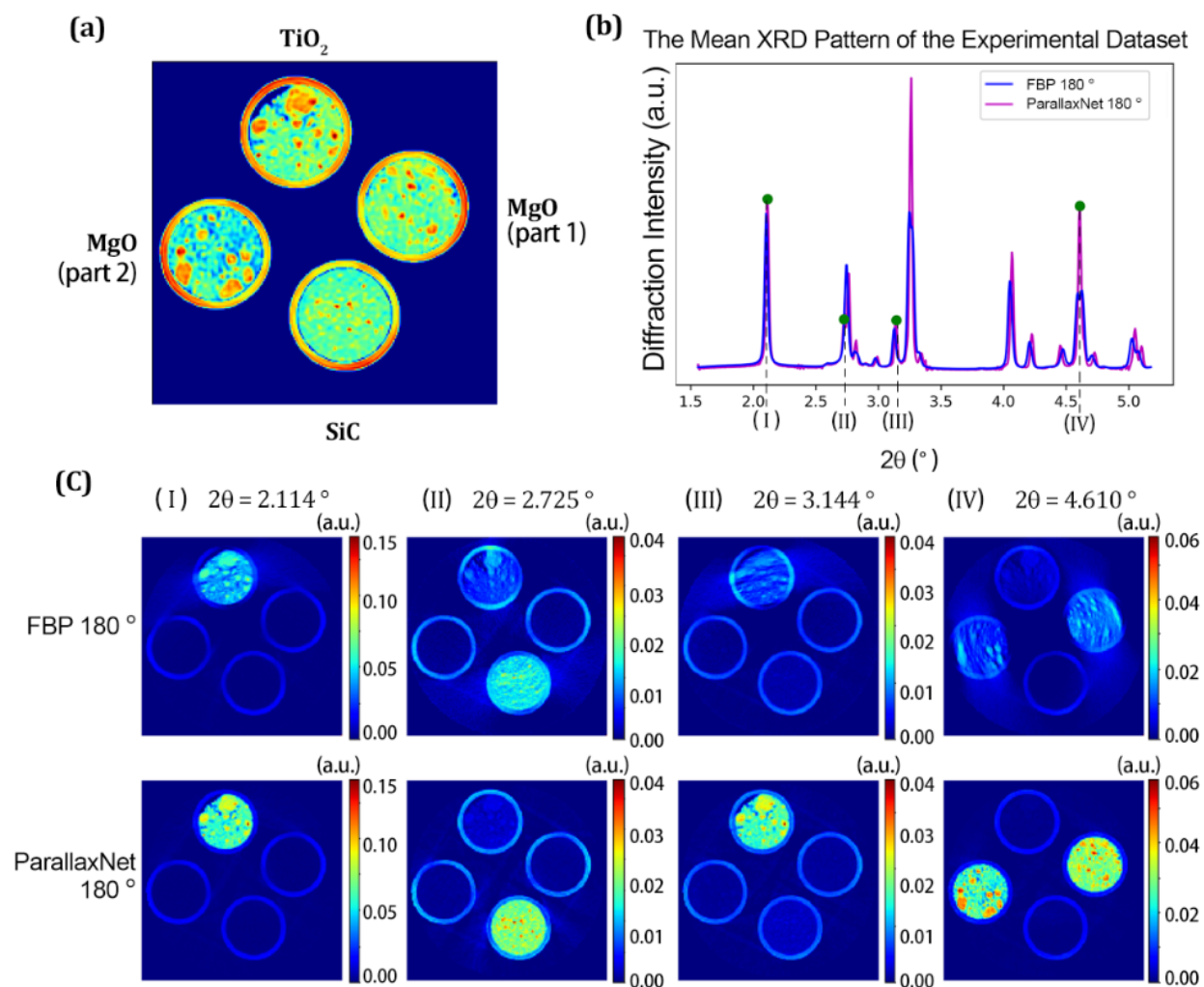
Figure 6. (a) The mean image of the Phantom XRD-CT dataset which contains crystalline TiO$_2$, MgO, and SiC. (b) The average diffraction patterns of FBP and ParallaxNet were reconstructed by 0-180 ° scans. (c) Selected interesting diffraction channels which are marked in (b).

Selected reflections corresponding to each of the three phases are shown in Figure 7. It can be clearly observed that the XRD-CT reflections reconstructed by FBP from both 180 and 360 ° scans exhibit significant peak broadening artefacts. Additionally, the diffraction peaks generated by FBP with 180 ° scan range exhibit peak shifting artefacts. In contrast, the diffraction peaks generated with 360 ° scan range using FBP are in good alignment with the ones obtained by the ParallaxNet with 180 ° scan range. This demonstrates that Parallax effectively reduces various artefacts brought about by parallax and also that it simply requires a 0-180 ° scan range to reconstruct parallax artefact-free data.
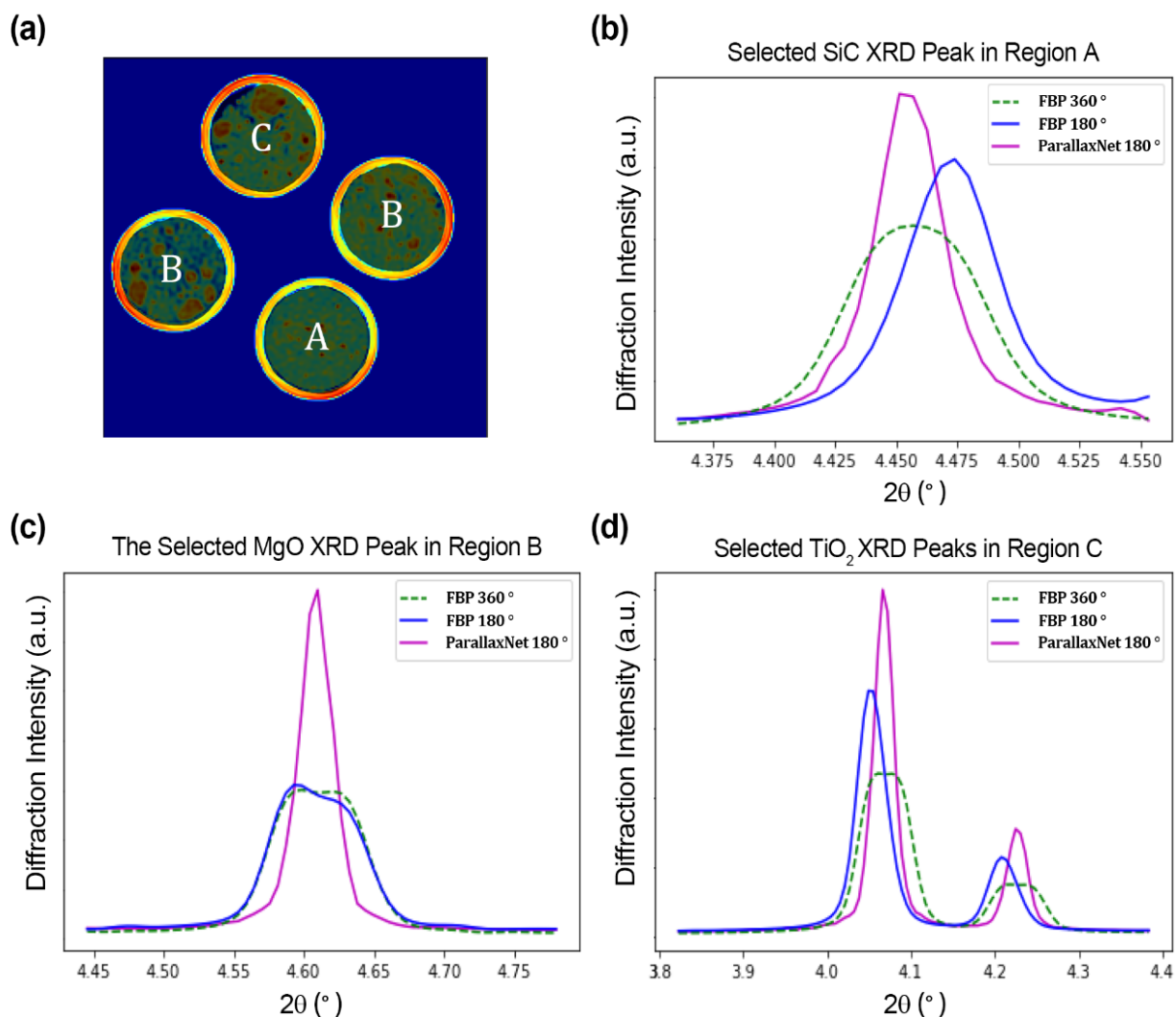
Figure 7. (a) The mean image of the Phantom XRD-CT dataset with three marked regions. (b) A selected peak of the average diffraction pattern in Region A. (c) A selected diffraction peak from the average diffraction pattern in Region B. (d) A selected peak from the average diffraction pattern in Region C. This figure shows the ParallaxNet can solve the peak broadening artefacts, and peak positions reconstructed by the ParallaxNet with 0-180 ° scans are aligned with the FBP reconstructed with 0-360 ° scans. In contrast, the FBP reconstructed diffraction peaks over the 0-180 ° scan range exhibit significant diffraction peak shifting which was caused by the parallax artefacts.

The Rietveld analysis of the reconstructed volumes further demonstrates the efficacy of our method. From the lattice parameter maps shown in Figure 8, it can be clearly seen that the lattice parameter maps from the ParallaxNet with 180 ° scans have almost identical values with those from the maps of the FBP derived from the 360 ° scan range. FBP images reconstructed

using 360 ° scan range should not exhibit any peak shifting, even when significant parallax artefacts are present; to clarify, the centroid position of the peaks will be in the correct position as if it were a dataset without parallax. As such, the lattice parameter maps of the ParallaxNet can be considered close to the ground truth. It is also worth mentioning that the ParallaxNet maps exhibit less noise compared to those from the FBP. The distribution of the lattice parameters is shown in histograms in Figure S6.
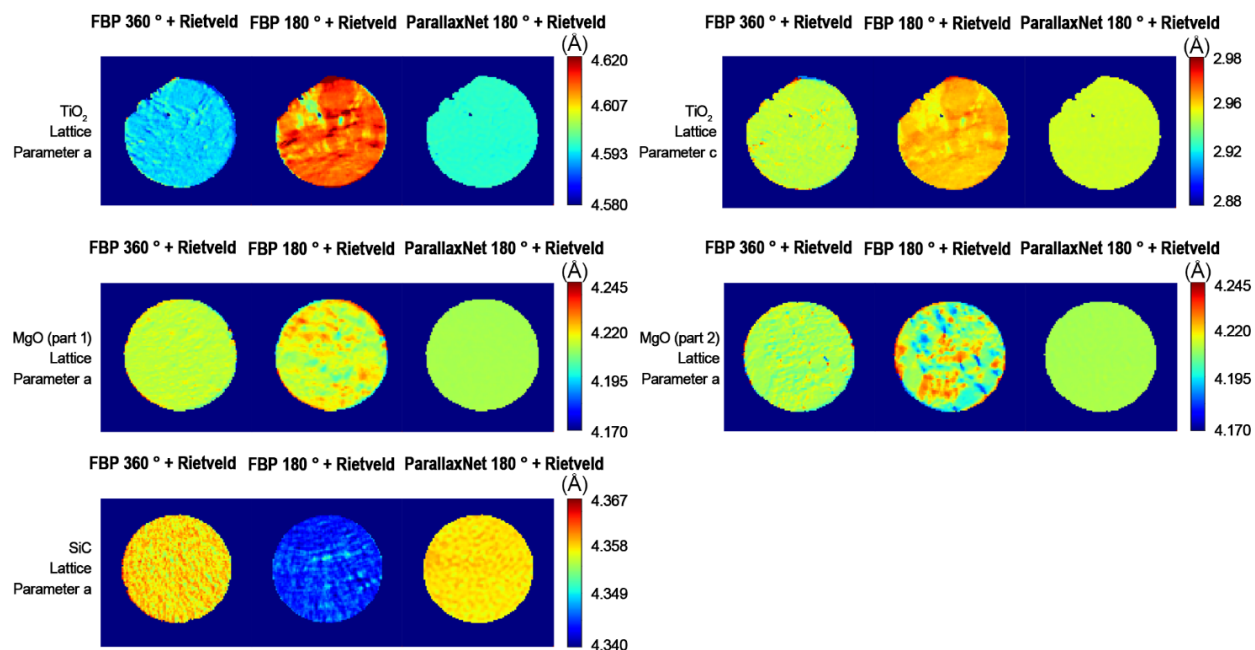


Figure 8. Lattice parameter maps associated with the four components shown in Figure 7 (a).

Figure 9 presents the scale factor and crystallite size maps obtained from the Rietveld analysis. A key observation is that the parallax artefact significantly affects the crystallite sizes obtained by conventional approaches. Specifically, on both 180 and 360 ° XRD-CT scans, it leads to broadened diffraction peaks and reduced crystallite values when using the FBP reconstruction algorithm. The maps suggest that ParallaxNet has, to a certain extent, solved the peak broadening artefact instigated by parallax. This correction is particularly pronounced for the two MgO components, where their crystallite sizes offer mutual validation. Based on these observations, we can deduce that ParallaxNet can correctly solve the parallax artefact on the real phantom experimental dataset. The $R_{wp}$ map, for all Rietveld analyses, can be further observed in Figure S7.
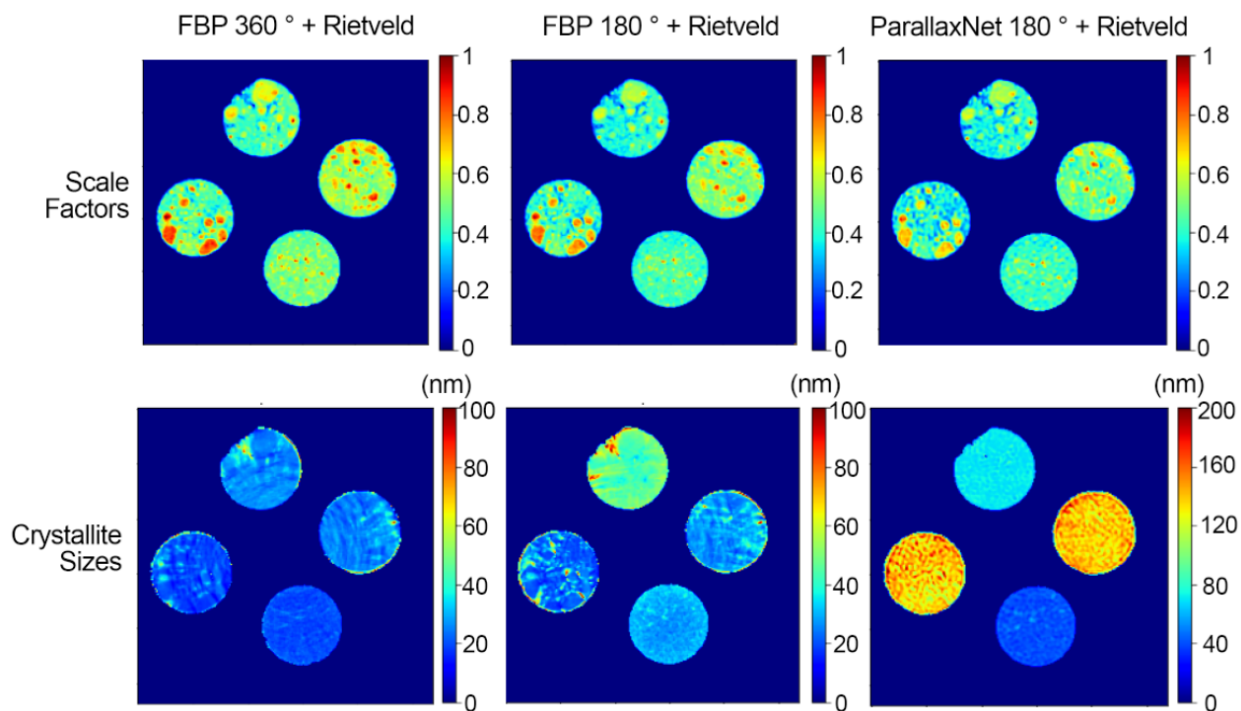
Figure 9. Top row: Scale factor maps (normalized) associated with four components. Button row: Crystallite size maps associated with four components.

## NMC532 cylindrical Li ion battery

In addition to the phantom dataset presented in the previous section, the efficacy of the method was evaluated with a second experimental dataset. Specifically, a dataset acquired from a commercially available and industrially relevant 10440 NMC532 Li-ion battery was used [44]. This dataset consisted of 521 translation steps, 1000 projections and 1800 channels of sinograms. To train this big dataset, we divided it into batches of 55 channels, and each batch took ca. 8 h to process using 5000 epochs. To address this large dataset, we first selected an XRD diffraction peak from the Cu phase and reconstructed only the images without parallax corresponding to this peak within the 55-channel range. Then, we performed Rietveld analysis on this 521 x 521 x 55 XRD-CT dataset to get the chemical information of the Cu phase presented in this Li-ion battery dataset. The original dataset was performed using a 0-360 ° scan range, but for testing the ParallaxNet, we only used the part of the data corresponding to the 0-180 ° scan range so for each batch, the size of the reference sinogram was 521 x 500 x 55. For a comparison, the XRD-CT data were also reconstructed using the FBP algorithm using both the 180 and 360 ° ranges and were analysed using the Rietveld method i.e. on the 55 selected channels of the Cu XRD peak (hkl reflection (111)). The ParallaxNet also utilized the FBP with 180° projections to pre-train the generator for faster convergence.

Figure 10a displays the average image from the selected 55 channels of the Cu XRD (111) peak, highlighting three regions of interest. Figures 10b-d depict the average XRD peaks from the marked regions. As illustrated in the figure, ParallaxNet can accurately reconstruct the Cu peak, producing a significantly sharper peak. The peak positions align with the XRD-CT data reconstructed by the FBP from the full 360 ° scan. This result shows that the ParallaxNet correctly removed both the peak shifting and broadening artefacts caused by the Parallax on this Cu XRD peak. It is important to note here that the centers of the peaks obtained from the FBP 360 ° scan align with those of the ParallaxNet-reconstructed peaks. However, it becomes evident that the peak shape cannot be effectively described using a single peak shape model. This observation is distinctly apparent across all peaks illustrated in Figure 10, with a particularly noticeable manifestation in the Cu diffraction peak from Region B. This observation bears significance, as attempting to fit these peaks using a single model, such as Gaussian or pseudo-Voigt models—commonly employed in XRD data analysis—can potentially yield inaccurate data interpretations. Such an approach might result in artificial shifts of the peaks, given that the employed model does not adequately capture the intricacies of the data's true behavior. This is especially crucial when high precision is required for the calculated lattice parameter values, *e.g.* in the order of $<10^{-3}$ Å such as when attempting to capture shifts in the Cu peak introduced by temperature gradients in these battery systems [57].
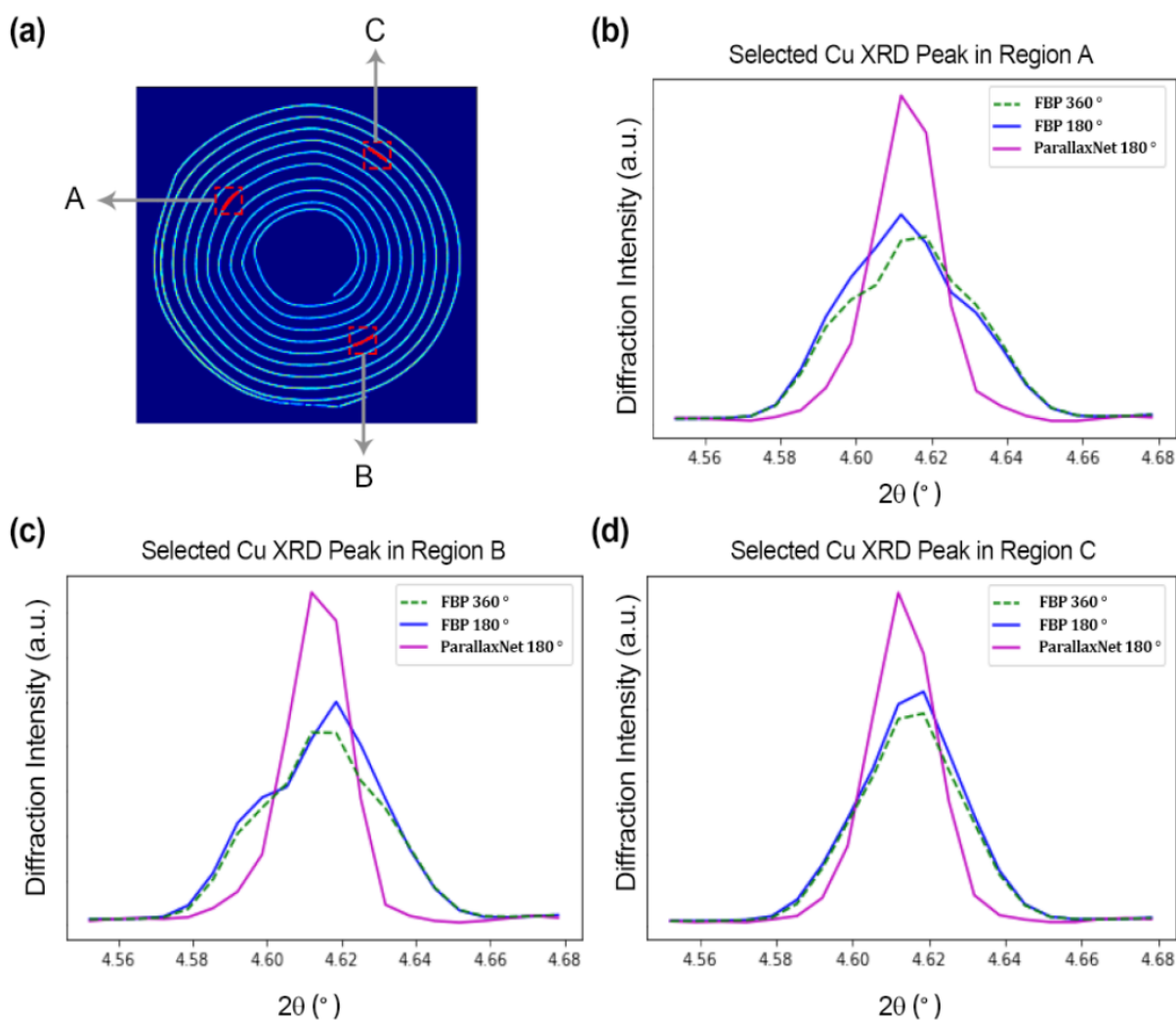
Figure 10. (a) The mean image of the Cu phase of Li-ion battery XRD-CT dataset with three marked regions. (b) The selected peak of the average diffraction pattern in Region A. (c) The selected peak of the average diffraction pattern in Region B. (d) The selected peak of the average diffraction pattern in Region C. This figure shows that ParallaxNet can solve the peak broadening and peak splitting artefacts.

Figure 11a displays the lattice parameter maps obtained through Rietveld analysis. As seen in the FBP with the 180 ° scan range lattice parameter map, the parallax artefact results in unevenly distributed lattice parameter values (as determined by the Rietveld analysis) across different positions of the same material (Cu phase). However, both the FBP with the 360 ° scan range and the ParallaxNet results with 180 ° scan range yield lattice parameter maps that are evenly distributed across all positions. The histogram depicting the distribution of lattice parameters for the three maps is shown in Figure 11b. The mean values of the lattice

parameters for the FBP with 360 ° scan range, the FBP with 180 ° scan range, and the ParallaxNet result are 3.6047 Å, 3.6045 Å, and 3.6048 Å, respectively. The scale factor maps and the $R_{wp}$ from the Rietveld analysis maps can be found in Figures S8 and S9.
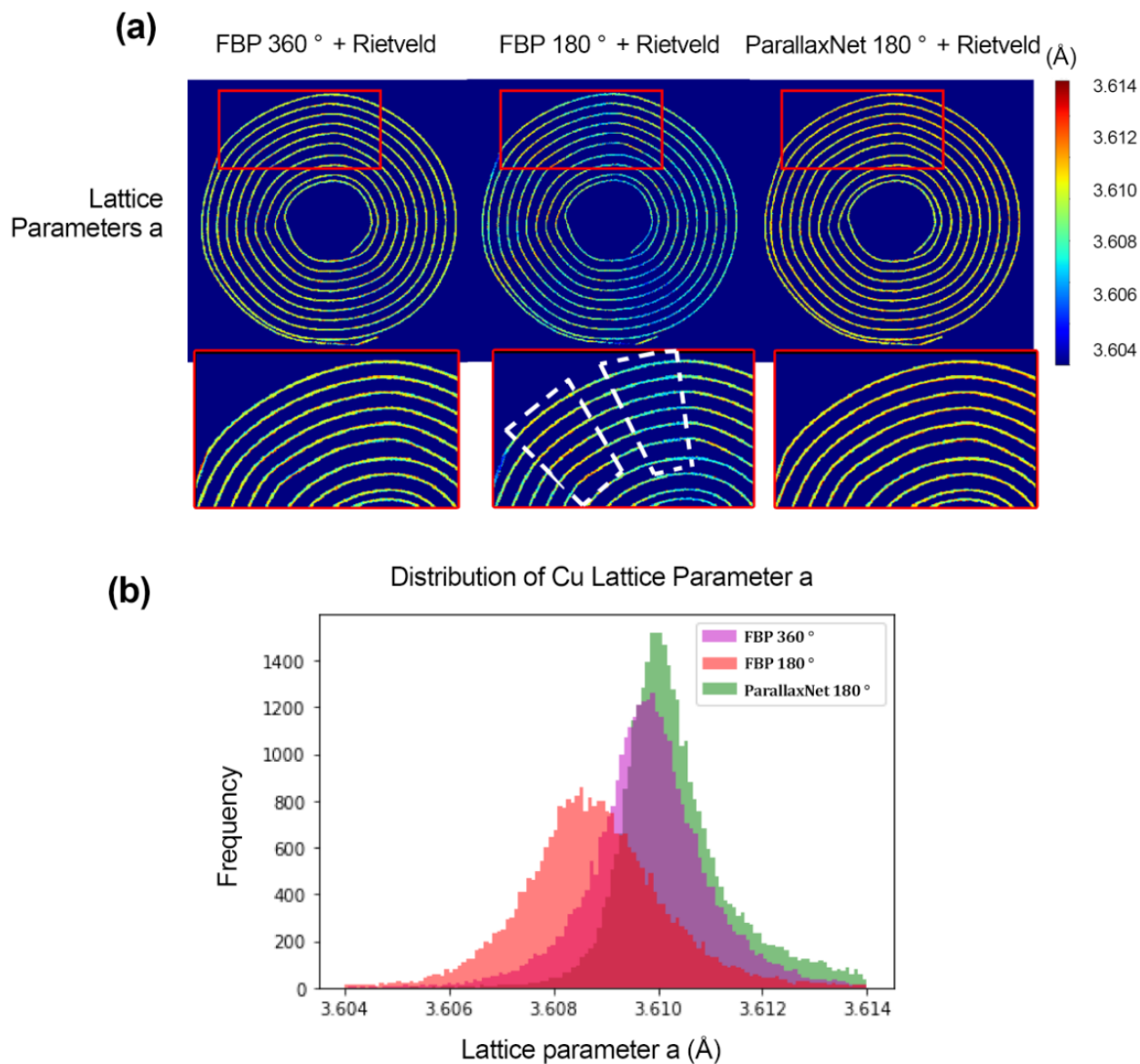


Figure 11. (a) The lattice parameter *a* maps obtained by Rietveld method for a Li-ion battery dataset. (b) the distribution of lattice parameters for the maps shown in (a).

It was therefore demonstrated that ParallaxNet can accurately reconstruct XRD-CT images/diffraction patterns of this experimental Li-ion dataset and that it is possible to extract meaningful chemical information from just a single peak of the XRD pattern. Subsequently, a broader range of diffraction channels was chosen, encompassing 555 out of the 1800 channels from the original dataset. These channels span a native $2\theta$ value range from 1.203 to 4.877 °. We divided these 555 channels into 11 segments, each containing 55 channels, consistent with the phantom dataset approach. To mitigate edge effects between the reconstructed images of each batch, we incorporated a 5-pixel overlap on either side of each segment. We then averaged the overlapping sections to produce the final XRD-CT image volume with dimensions of 521 x 521 x 555.

To reconstruct this expanded dataset, ParallaxNet required 90 h of training time, which includes both initialization and pre-training with FBP. Since each batch is independent, we utilized three NVIDIA Quadro RTX8000 GPUs to process these 11 batches in parallel using PyTorch. In the end, it took ca. 33 real-world h to complete this dataset. It's worth noting that this represents the most extreme scenario encountered in real-world experimental datasets, and the DLSR method cannot handle a dataset of this magnitude.

Figure 12 shows the NMC532 phase of the reconstructed dataset, highlighting three specific regions of interest. Additionally, this figure displays the selected average XRD peaks corresponding to the NMC532 phase. Other NMC532 peaks of these three regions are also shown in Figure S10. These figures confirm that ParallaxNet can accurately reconstruct the same peak positions as those derived from the FBP reconstructed with the 360 ° scan range. Furthermore, ParallaxNet effectively addresses the issue of peak broadening artefacts, producing peaks that are sharper and narrower compared to those in the FBP images.
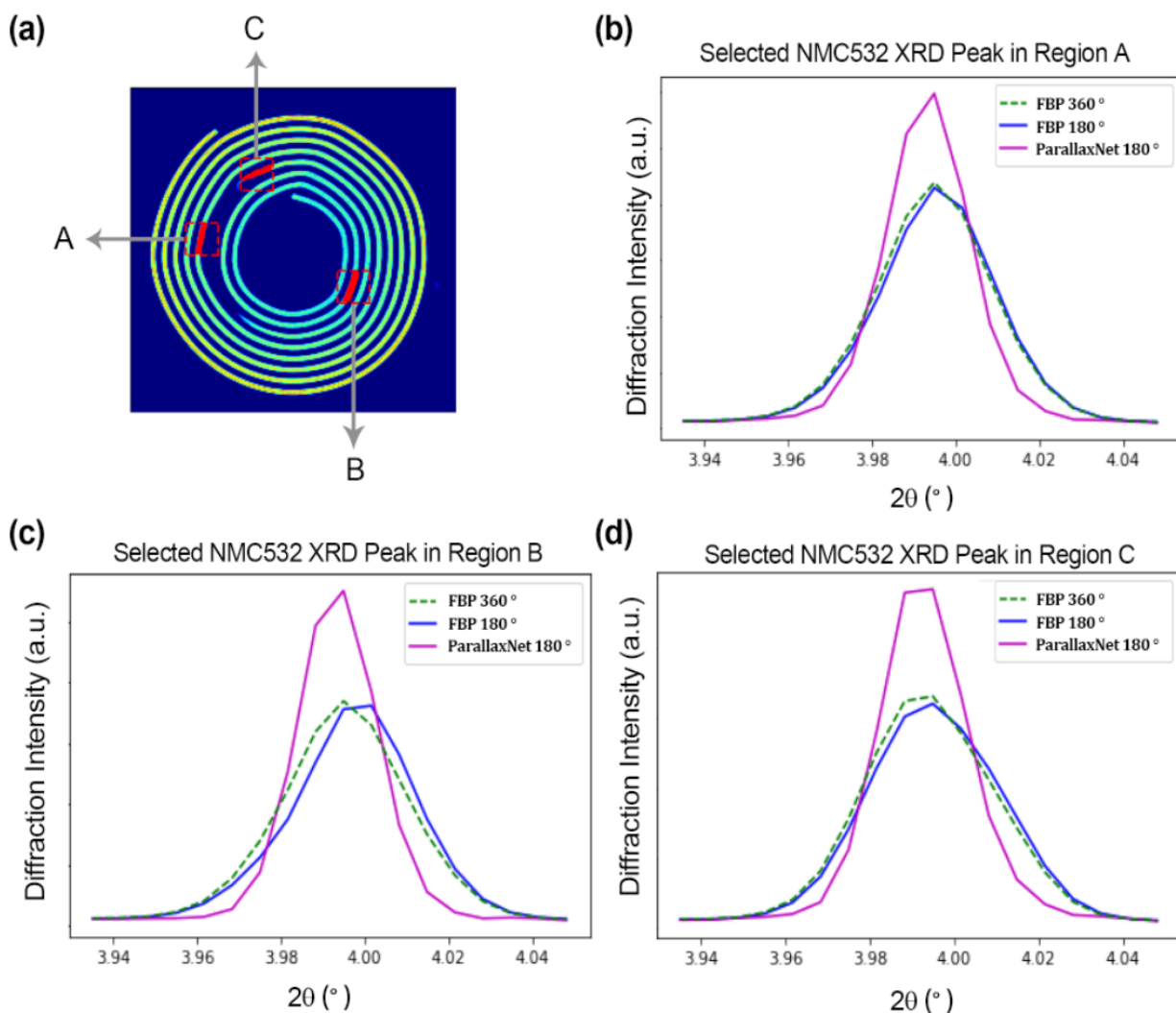
Figure 12. (a) The mean image of the NMC532 phase of Li-ion battery XRD-CT dataset with three marked regions. (b) The selected peak of the average diffraction pattern in Region A. (c) The selected peak of the average diffraction pattern in Region B. (d) The selected peak of the average diffraction pattern in Region C. This figure shows that ParallaxNet can solve the peak broadening artefacts, and reconstruct correct peak positions compared to the FBP with 0-180 ° scan range.

Maps obtained from the Rietveld analysis of the NMC532 phases are shown in Figure 13 and Figure S11. The crystallite sizes obtained with the three different methods on the top line of Figure 13 indicate the crystallite sizes calculated from the ParallaxNet reconstructed volume are larger than both FBP methods with 180 and 360 ° scans respectively. The average crystallite sizes raised from ca. 91 nm (for FBP with 180 ° scans) and 92 nm (for FBP with 360 ° scans) to 137 nm (for the ParallaxNet), which also supports the conclusion we drew from visual

inspection: the diffraction peaks are sharper and narrower than those produced by conventional methods. The $R_{wp}$ maps of the Rietveld analysis are shown in Figure S12.

The lattice parameter maps of the NMC532 phase also indicate that the ParallaxNet can correctly reconstruct the evenly distributed lattice parameter maps which aligns with the FBP with 360 ° scan. The peak shifting artefact in the images reconstructed by the FBP with 180 ° scan range has been effectively eliminated by ParallaxNet. The distribution of the lattice parameters of the NMC532 is presented in Figure S13.
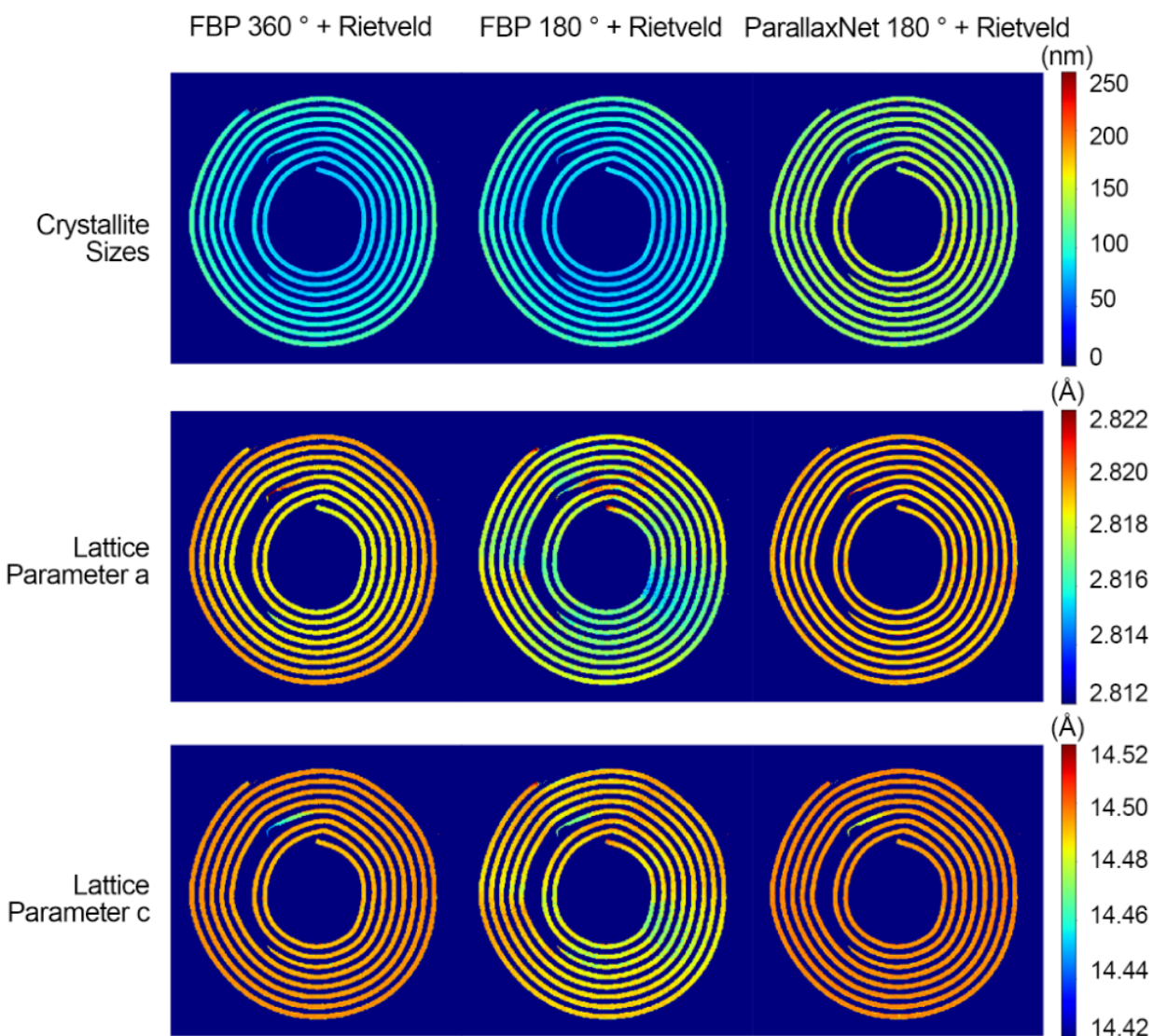


Figure 13. Top row: crystallite size maps of the NMC532 phase. Mid row: lattice parameter *a* maps of the NMC532 phase. Bottom Row: lattice parameter c maps. All maps are obtained by Rietveld analysis on the Li-ion battery XRD-CT dataset.

# Summary & Conclusions

In this paper, we introduced a novel and robust XRD-CT reconstruction approach, ParallaxNet, designed to reconstruct images from XRD-CT data containing parallax artefacts. The ParallaxNet strategy employs a 3D neural network generator framework, SD2Vol, together with a customized forward projector to produce parallax artefact-free images/diffraction patterns. This is achieved through an iterative approach by comparing the difference between the generated sinogram volume and the input reference sinogram volume. We evaluated ParallaxNet's performance using three datasets: a simulated XRD-CT dataset, an experimental XRD-CT dataset acquired using a phantom object and an experimental XRD-CT dataset recorded on an NMC532 cylindrical Li-ion battery.

For all three datasets, this new approach accurately reconstructed the peak positions using only 0-180 ° angular range, eliminating the need for a 0-360 ° scan which halves the required acquisition time (i.e. half the number of projections). Furthermore, the reconstructed peaks were sharper and narrower than those produced by traditional FBP methods, both with 180 and 360 ° scans. It should also be noted that in this work it was also shown that simply using a 360 ° scan approach as a means to remove parallax artefacts is insufficient and should be avoided as it leads to peaks with shapes that cannot be modeled with a single profile (*e.g.* Gaussian peak). This was clearly demonstrated with the experimental XRD-CT presented in this work, an example being the Cu component in the cylindrical Li-ion battery. ParallaxNet overcomes the peak shape problems associated with the 0-360 ° scan approach and also presents distinct advantages over the previously developed DLSR methodology, which is to the best of our knowledge the only alternative solution to removing parallax artefacts in XRD-CT data, addressing several inherent limitations:

- Firstly, ParallaxNet operates without requiring *a priori* knowledge about the chemical composition of the sample being measured.
- DLSR also requires the identification of all phases and the construction of a robust physical model; this can potentially lead to some minor components being overlooked during the inspection of diffraction patterns in the sinogram data.
- Furthermore, ParallaxNet is more scalable. In this work, we applied the ParallaxNet on the full size experimental phantom XRD-CT datasets. However, the DLSR can only be applied on the scaled-down version of the same dataset(s) as shown in the DLSR paper (*e.g.* with 121 x 121 image sizes for the Li ion battery). Moreover, ParallaxNet does not need as much RAM requirements as the DLSR approach, especially when DLSR is used in conjunction with TOPAS version 7.

- ParallaxNet does not require any data preprocessing. ParallaxNet can be applied on the raw sinograms, but DLSR needs the manually created masks for each phase and background subtraction on the sinograms in order to use a simple background model.
- We have demonstrated that the conventional method of employing a 0-360 ° scan with FBP to eliminate parallax artefacts and obtain precise lattice parameter values can be precarious. For instance, the FBP reconstruction of the Cu peaks in the 0-360 ° scan revealed peaks that cannot be modeled using a single peak shape model (such as Gaussian or pseudo-Voigt). This could potentially result in wrong lattice parameter values and misinterpretation of the data, especially if lattice parameter values with high precision are required to be extracted from the data.

At this stage, while ParallaxNet presents a promising approach to XRD-CT image reconstruction with parallax artefact, it is not without its limitations. A significant constraint is the extended computational time required for large datasets. For instance, the Li-ion dataset, with sinogram dimensions of 521 x 500 x 540, demanded a staggering 90 hours of computational time. Currently, due to GPU memory constraints, there's a necessity to divide datasets into smaller batches for processing. Moving forward, there is potential to explore a more streamlined generator, which could significantly minimize the computational resources needed and address some of these challenges. Last but not least, it should be noted that the developed method can be applied to other X-ray scattering-based computed tomography data suffering from parallax artefacts, such as pair distribution computed tomography.


## Methods & Materials

The powder samples measured in this work were SiC (nanopowder, <100 nm particle size, 594911-100G, Sigma-Aldrich), $TiO_2$ Rutile (204757-25G, Sigma-Aldrich) and MgO (307742-500G, Sigma-Aldrich). The three powder samples were mounted into separate glass pipettes with an outer diameter of ca. 7.5 mm supported by quartz wool from both ends. Two pipettes were prepared using the same MgO powder sample. The four glass pipettes containing the powder samples were mounted onto a 3D printed sample holder designed for the parallax experiment. Photographs of the experimental setup can be found in our previous work [51].

XRD-CT measurements of the phantom sample were performed at beamline station P07 (EH2) at PETRA III, DESY, using a 103.5 keV (λ = 0.11979 Å) monochromatic X-ray beam focused to a spot size of 20 × 3 μm (H × V). 2D powder diffraction patterns were collected using a Pilatus3 X CdTe 2 M hybrid photon counting area detector. The 3D printed sample holder was mounted directly on the rotation stage. The rotation stage was mounted perpendicularly to a hexapod; the hexapod was used to translate the sample across the beam. The XRD-CT scans were

measured by performing a series of zigzag line scans in the z (vertical) direction using the hexapod and rotation steps.

Two XRD-CT scans were performed, in both cases the number of translation steps were 300 with a 80 µm step size and a 10 ms exposure time per point. The first XRD-CT scan was performed over a 0-180 ° range while the second over a 0-360 ° range, both using 300 angular steps. The second sample was a pristine (as-received) 10440 Li-ion NMC532 Trustfire cylindrical battery [44] and it was scanned using the same beamline and experimental setup using a 73.89 keV ($\lambda$ = 0.16779 Å) monochromatic X-ray beam focused to the same spot size of $20 \times 3$ µm. An XRD-CT dataset was acquired using 521 translation steps with a 20 µm step size and a 10 ms exposure time per point. The XRD-CT scan was performed over a 0-360 ° range using 1000 angles in total.

The detector calibration was performed using a $CeO_2$ standard. Every 2D diffraction image was calibrated and azimuthally integrated to a 1D powder diffraction pattern with a 10 % trimmed mean filter using the pyFAI software package, nDTomo software and in-house developed scripts [58–60]. The integrated diffraction patterns were reshaped into sinograms and centered; the air scatter signal was subtracted from the data. For the conventional data analysis approach, the XRD-CT images (i.e. reconstructed data volume) were reconstructed using the FBP algorithm. A pseudo-voigt peak shape function was used for the refinements after the analysis of the $CeO_2$ pattern. Rietveld analysis was performed on the reconstructed diffraction patterns with the TOPAS software version 7 [52] on a voxel by voxel basis. Rietveld analysis was first performed using the summed diffraction pattern of each XRD-CT dataset (i.e. to provide a good starting model) before running the voxel-by-voxel Rietveld analysis to provide the spatially-resolved physico-chemical information. The parameters refined were the scale factor, lattice parameter and crystallite size for each phase. A 2nd order Chebyshev polynomial was used to model the background as it was fairly flat in all reconstructed patterns. A workstation with an Intel Xeon W-2155 CPU, a NVidia Quadro RTX8000 GPU, and 128 GB of RAM was used to perform the ParallaxNet and full profile analysis on all datasets presented in the paper.

## Author Contributions

HD and AV developed ParallaxNet with contributions and discussions with KTB, SDMJ and AMB. OG, ACD and MZ were responsible for P07 instrumentation and setup at the PETRA III, DESY. The XRD-CT data were analysed by HD and AV. HD and AV are responsible for writing the manuscript with feedback given by all contributors.

# Acknowledgements

# Data Availability

The integrated XRD-CT data presented in this work, both simulated and experimental, have been made publicly available through an open access repository and can be found here: https://zenodo.org/record/8344637

# Code Availability

The code developed in this work is available from the authors upon reasonable request.

# Conflicts of interest

The authors declare no conflicts of interest.

# References

1. Esteva, A. *et al.* Deep learning-enabled medical computer vision. *Npj Digit. Med.* **4**, 1–9 (2021).

2. LeCun, Y., Bengio, Y. & Hinton, G. Deep learning. *Nature* **521**, 436–444 (2015).

3. Jiao, L. & Zhao, J. A survey on the new generation of deep learning in image processing. *Ieee Access* **7**, 172231–172263 (2019).

4. Voulodimos, A., Doulamis, N., Doulamis, A. & Protopapadakis, E. Deep learning for computer vision: A brief review. *Comput. Intell. Neurosci.* **2018**, (2018).

5. Cambria, E. & White, B. Jumping NLP curves: A review of natural language processing research. *IEEE Comput. Intell. Mag.* **9**, 48–57 (2014).

6. Olsson, F. A literature survey of active machine learning in the context of natural language processing. (2009).

7. Ahishakiye, E., Bastiaan Van Gijzen, M., Tumwiine, J., Wario, R. & Obungoloch, J. A survey on deep learning in medical image reconstruction. *Intell. Med.* **01**, 118–127 (2021).

8. Wang, G., Ye, J. C. & De Man, B. Deep learning for tomographic image reconstruction. *Nat. Mach. Intell.* **2**, 737–748 (2020).

9. Zhang, M., Gu, S. & Shi, Y. The use of deep learning methods in low-dose computed tomography image reconstruction: a systematic review. *Complex Intell. Syst.* **8**, 5545–5561 (2022).

10. Bracewell, R. N. & Riddle, A. C. Inversion of Fan-Beam Scans in Radio Astronomy. *Astrophys. J.* **150**, 427 (1967).

11. Beister, M., Kolditz, D. & Kalender, W. A. Iterative reconstruction methods in X-ray CT. *Phys. Med.* **28**, 94–108 (2012).

12. Pan, X., Sidky, E. Y. & Vannier, M. Why do commercial CT scanners still employ traditional, filtered back-projection for image reconstruction? *Inverse Probl.* **25**, 123009 (2009).

13. Chetih, N. & Messali, Z. Tomographic image reconstruction using filtered back projection (FBP) and algebraic reconstruction technique (ART). in *2015 3rd International Conference on Control, Engineering & Information Technology (CEIT)* 1–6 (IEEE, 2015).

14. Solomon, J., Lyu, P., Marin, D. & Samei, E. Noise and spatial resolution properties of a commercially available deep learning-based CT reconstruction algorithm. *Med. Phys.* **47**, 3961–3971 (2020).

15. Higaki, T. *et al.* Deep learning reconstruction at CT: phantom study of the image characteristics. *Acad. Radiol.* **27**, 82–87 (2020).

16.    Yaqub, M. *et al.* Deep Learning-Based Image Reconstruction for Different Medical Imaging Modalities. *Comput. Math. Methods Med.* **2022**, e8750648 (2022).

17.    Zhu, B., Liu, J. Z., Cauley, S. F., Rosen, B. R. & Rosen, M. S. Image reconstruction by domain-transform manifold learning. *Nature* **555**, 487–492 (2018).

18.    Rodriguez, A. F., Blass, W. E., Missimer, J. H. & Leenders, K. L. Artificial neural network Radon inversion for image reconstruction. *Med. Phys.* **28**, 508–514 (2001).

19.    Paschalis, P. *et al.* Tomographic image reconstruction using Artificial Neural Networks. *Nucl. Instrum. Methods Phys. Res. Sect. Accel. Spectrometers Detect. Assoc. Equip.* **527**, 211–215 (2004).

20.    Argyrou, M., Maintas, D., Tsoumpas, C. & Stiliaris, E. Tomographic Image Reconstruction based on Artificial Neural Network (ANN) techniques. in *2012 IEEE Nuclear Science Symposium and Medical Imaging Conference Record (NSS/MIC)* 3324–3327 (2012). doi:10.1109/NSSMIC.2012.6551757.

21.    Würfl, T., Ghesu, F. C., Christlein, V. & Maier, A. Deep Learning Computed Tomography. in *Medical Image Computing and Computer-Assisted Intervention - MICCAI 2016* (eds. Ourselin, S., Joskowicz, L., Sabuncu, M. R., Unal, G. & Wells, W.) 432–440 (Springer International Publishing, 2016).

22.    Ge, Y. *et al.* ADAPTIVE-NET: deep computed tomography reconstruction network with analytical domain transformation knowledge. *Quant. Imaging Med. Surg.* **10**, 415–427 (2020).

23.    Ma, G., Zhu, Y. & Zhao, X. Learning Image From Projection: A Full-Automatic Reconstruction (FAR) Net for Computed Tomography. *IEEE Access* **8**, 219400–219414 (2020).

24.    Yang, X. & Schroer, C. Strategies of Deep Learning for Tomographic Reconstruction. in *2021 IEEE International Conference on Image Processing (ICIP)* 3473–3476 (2021).

doi:10.1109/ICIP42928.2021.9506395.

25.     Harding, G., Kosanetzky, J. & Neitzel, U. X-ray diffraction computed tomography. *Med.*
        *Phys.* **14**, 515–525 (1987).

26.     Kleuker, U., Suortti, P., Weyrich, W. & Spanne, P. Feasibility study of x-ray diffraction
        computed tomography for medical imaging. *Phys. Med. Biol.* **43**, 2911 (1998).

27.     Beale, A. M., Jacques, S. D., Gibson, E. K. & Di Michiel, M. Progress towards five
        dimensional diffraction imaging of functional materials under process conditions. *Coord.*
        *Chem. Rev.* **277**, 208–223 (2014).

28.     Omori, N. E., Bobitan, A. D., Vamvakeros, A., Beale, A. M. & Jacques, S. D. M. Recent
        developments in X-ray diffraction/scattering computed tomography for materials science.
        *Philos. Trans. R. Soc. Math. Phys. Eng. Sci.* **381**, 20220350 (2023).

29.     Mürer, F. K. *et al.* 3D maps of mineral composition and hydroxyapatite orientation in
        fossil bone samples obtained by X-ray diffraction computed tomography. *Sci. Rep.* **8**, 10052
        (2018).

30.     Vamvakeros, A. *et al.* Real-time multi-length scale chemical tomography of fixed bed
        reactors during the oxidative coupling of methane reaction. *J. Catal.* **386**, 39–52 (2020).

31.     Middelkoop, V. *et al.* 3D printed Ni/Al2O3 based catalysts for CO2 methanation-a
        comparative and operando XRD-CT study. *J. CO2 Util.* **33**, 478–487 (2019).

32.     Matras, D. *et al.* Operando and postreaction diffraction imaging of the La–Sr/CaO
        catalyst in the oxidative coupling of methane reaction. *J. Phys. Chem. C* **123**, 1751–1760
        (2019).

33.     Wragg, D. S. *et al.* Mapping the coke formation within a zeolite catalyst extrudate in
        space and time by operando computed X-ray diffraction tomography. *J. Catal.* **401**, 1–6
        (2021).

34. Matras, D. *et al.* Effect of thermal treatment on the stability of Na-Mn-W/SiO 2 Catalyst for the Oxidative Coupling of Methane. *Faraday Discuss.* (2020).

35. Matras, D. *et al.* In situ X-ray diffraction computed tomography studies examining the thermal and chemical stabilities of working Ba 0.5 Sr 0.5 Co 0.8 Fe 0.2 O 3- δ membranes during oxidative coupling of methane. *Phys. Chem. Chem. Phys.* **22**, 18964–18975 (2020).

36. Vamvakeros, A. *et al.* Real-time tomographic diffraction imaging of catalytic membrane reactors for the oxidative coupling of methane. *Catal. Today* (2020).

37. Martens, I. *et al.* Imaging heterogeneous electrocatalyst stability and decoupling degradation mechanisms in operating hydrogen fuel cells. *ACS Energy Lett.* **6**, 2742–2749 (2021).

38. Li, T. *et al.* Design of next-generation ceramic fuel cells and real-time characterization with synchrotron X-ray diffraction computed tomography. *Nat. Commun.* **10**, 1497 (2019).

39. Sottmann, J. *et al.* Chemical Structures of Specific Sodium Ion Battery Components Determined by Operando Pair Distribution Function and X-ray Diffraction Computed Tomography. *Angew. Chem. Int. Ed.* **56**, 11385–11389 (2017).

40. Tonin, G. *et al.* Operando investigation of the lithium/sulfur battery system by coupled X-ray absorption tomography and X-ray diffraction computed tomography. *J. Power Sources* **468**, 228287 (2020).

41. Liu, H. *et al.* Quantifying reaction and rate heterogeneity in battery electrodes in 3D through operando X-ray diffraction computed tomography. *ACS Appl. Mater. Interfaces* **11**, 18386–18394 (2019).

42. Finegan, D. P. *et al.* Spatially resolving lithiation in silicon–graphite composite electrodes via in situ high-energy x-ray diffraction computed tomography. *Nano Lett.* **19**, 3811–3820 (2019).

43. Finegan, D. P. *et al.* Spatial quantification of dynamic inter and intra particle crystallographic heterogeneities within lithium ion electrodes. *Nat. Commun.* **11**, 1–11 (2020).

44. Vamvakeros, A. *et al.* Cycling Rate-Induced Spatially-Resolved Heterogeneities in Commercial Cylindrical Li-Ion Batteries. *Small Methods* **5**, 2100512 (2021).

45. Petz, D. *et al.* Lithium distribution and transfer in high-power 18650-type Li-ion cells at multiple length scales. *Energy Storage Mater.* **41**, 546–553 (2021).

46. Matras, D. *et al.* Emerging chemical heterogeneities in a commercial 18650 NCA Li-ion battery during early cycling revealed by synchrotron X-ray diffraction tomography. *J. Power Sources* **539**, 231589 (2022).

47. Vamvakeros, A. *et al.* 5D operando tomographic diffraction imaging of a catalyst bed. *Nat. Commun.* **9**, 1–11 (2018).

48. Matras, D. *et al.* Multi-length scale 5D diffraction imaging of Ni–Pd/CeO2–ZrO2/Al2O3 catalyst during partial oxidation of methane. *J. Mater. Chem. A* **9**, 11331–11346 (2021).

49. Sottmann, J. *et al.* 5D total scattering computed tomography reveals the full reaction mechanism of a bismuth vanadate lithium ion battery anode. *Phys. Chem. Chem. Phys.* **24**, 27075–27085 (2022).

50. Scarlett, N. V. Y., Rowles, M. R., Wallwork, K. S. & Madsen, I. C. Sample-displacement correction for whole-pattern profile fitting of powder diffraction data collected in capillary geometry. *J. Appl. Crystallogr.* **44**, 60–64 (2011).

51. Vamvakeros, A. *et al.* DLSR: a solution to the parallax artefact in X-ray diffraction computed tomography data. *J. Appl. Crystallogr.* **53**, (2020).

52. Coelho, A. A. TOPAS and TOPAS-Academic: an optimization program integrating computer algebra and crystallographic objects written in C++. *J. Appl. Crystallogr.* **51**, 210–218 (2018).

53.     Dong, H. *et al.* A scalable neural network architecture for self-supervised tomographic image reconstruction. *Digit. Discov.* (2023) doi:10.1039/D2DD00105E.

54.     Dong, J., Fu, J. & He, Z. A deep learning reconstruction framework for X-ray computed tomography with incomplete data. *PloS One* **14**, e0224426 (2019).

55.     Wang, Z., Bovik, A. C., Sheikh, H. R. & Simoncelli, E. P. Image quality assessment: from error visibility to structural similarity. *IEEE Trans. Image Process.* **13**, 600–612 (2004).

56.     van Aarle, W. *et al.* The ASTRA Toolbox: A platform for advanced algorithm development in electron tomography. *Ultramicroscopy* **157**, 35–47 (2015).

57.     Heenan, T. M. M. *et al.* Mapping internal temperatures during high-rate battery applications. *Nature* **617**, 507–512 (2023).

58.     Vamvakeros, A. *et al.* Removing multiple outliers and single-crystal artefacts from X-ray diffraction computed tomography data. *J. Appl. Crystallogr.* **48**, 1943–1955 (2015).

59.     A. Vamvakeros & H. Dong. nDTomo software suite. (2019). doi: https://doi.org/10.5281/zenodo.7139214, url: https://github.com/antonyvam/nDTomo.

60.     Ashiotis, G. *et al.* The fast azimuthal integration Python library: pyFAI. *J. Appl. Crystallogr.* **48**, 510–519 (2015).